ACI STRUCTURAL JOURNAL

A JOURNAL OF THE AMERICAN CONCRETE INSTITUTE

Prepublished Paper

This is a prepublished manuscript. The final manuscript is tentatively scheduled for V. 121, No. 4 and is subject to change.

The DOI for this paper is 10.14359/51740570 and will not change, but won't be activated until the issue has been published.

American Concrete Institute

P-M Interaction of Geopolymer FRC Slender Columns reinforced with Steel, GFRP or Hybrid Double-Layer

by Mohammad AlHamaydeh and Fouad Amin

Biography:

ACI member **AlHamaydeh** earned his Ph.D. in structural/earthquake engineering from the University of Southern California, USA. His research and expertise include nonlinear structural dynamic response analysis and modeling, passive control and supplemental damping devices, computer-aided design and simulation, nonlinear finite element methods, and soil-structure interaction. Prior to his academic career, he was an active member of the Structural Engineers Association of California (SEAOC) as a consultant engineer in Los Angeles, California. **Fouad** is a research assistant at the American University of Sharjah and an assistant lecturer at Mansoura University, Egypt.

ABSTRACT

A numerical integration model is developed to investigate the axial load-bending moment interactions of fiber-reinforced geopolymer concrete (FRGPC) columns reinforced with double layers of steel, glass fiber reinforced polymer (GFRP), or hybrid reinforcement. The model accounts for material and geometric nonlinearities, including the slenderness-induced second-order effects through an iterative layer-by-layer integration scheme of the critical section. Analytical investigations were conducted for various double-layer reinforcement configurations of steel, GFRP, and hybrid. The effect of adding steel/synthetic macro fibers to the concrete matrix was also investigated. Moreover, comprehensive deterministic sensitivity analyses were conducted to assess the influence of the concrete compressive strength (f_{co}), reinforcement fiber dosage, and the longitudinal/transverse reinforcement ratios on different response values. For the axial load capacity of GFRP-reinforced columns, the longitudinal reinforcement ratio was found to be the most influential parameter, while for the steel/hybrid reinforced columns, f_{co}, was the most influential parameter. Moreover, for all the simulated configurations, confinement efficiency was most sensitive to f_{co} out of all the investigated parameters. The longitudinal reinforcement ratio most influenced bending moment capacity and the associated secant stiffness. Lastly, axial load-bending moment interactions were developed for various reinforcement configurations. The interactions included the effects of the slenderness ratio, the macro fiber type, longitudinal/transverse reinforcement type/strength, and the longitudinal reinforcement ratio. The GFRP-reinforced columns showed more sensitivity to slenderness effects than steel-reinforced columns.

Keywords: fiber-reinforced concrete (FRC); geopolymer concrete (GPC); glass-fiber-reinforced polymer (GFRP) rebars; hybrid reinforcement; interaction diagrams; slender columns; slenderness ratio.

INTRODUCTION

In the 1970s, the term "geopolymer" was introduced by Davidovits [1] to describe a reaction of aluminosilicate powder with an alkaline solution. Geopolymers attain their strength through the polycondensation of silica and alumina with a high alkaline content [2]. Geopolymer concrete (GPC) can be produced by polymerizing aluminosilicates like slag, rice husk ash, fly ash, and metakaolin using an alkaline solution [3]. Incorporating ordinary Portland cement (OPC) into the reaction develops calcium silicate hydrates and the standard outputs of the geopolymer reaction to attain higher strength [4–6]. Production of OPC is responsible for about 10% of the total carbon dioxide global emissions (CO_2), which increases the greenhouse effect. Moreover, OPC production consumes virgin and non-renewable resources [7,8]. On the other hand, GPC ensures sustainability by reducing CO2 emissions by 80% and consuming 60% of the energy required, compared to OPC [9,10]. Moreover, GPC could reduce construction costs due to early strength gain [11].

Furthermore, GPC has been proven to have properties similar to or superior to OPC concrete. It has better resistance to chloride and sulfate attacks and can reach high strength values using slag and dolomite [6,12–14]. On exposure to fire, GPC has proven to have a low strength degradation, good spalling resistance, higher residual stress, and better splitting tensile strength retention than OPC concrete [15–17]. Also, it was reported that the flexural behavior of GPC was enhanced, and brittleness was reduced upon adding steel fibers to the concrete mix [18,19]. Adding randomly distributed short fibers to concrete can enhance compression post-peak behavior and significantly improve flexural performance. These fibers work as an inherent reinforcement that bridges the cracks and minimizes their propagation, thus resulting in a more ductile failure mode [20]. The effect of adding different volumetric ratios of reinforcement fibers, mainly steel and synthetic, causes an increase in concrete toughness and flexural strength [21]. It was also reported that changing the fibers' volumetric ratio does not essentially affect the pre-crack elastic response; however, its effects can be clearly seen in the post-crack behavior [20].

GPC has enhanced durability compared to OPC concrete [8]; however, concrete type is not the only parameter affecting structures' durability. In general, steel-reinforced concrete structures suffer from corrosion, which is a factor that can heavily affect their long-term durability. Driven by the need for an alternative material, fiber-reinforced polymer (FRP) rebars have been heavily studied and tested as longitudinal and transverse reinforcement. As a result, FRP reinforcement provides non-corrosive characteristics that can substantially increase the reinforced concrete's durability and reduce maintenance costs [22]. North American regulatory authorities and public agencies have included FRP rebars as corrosion-resistant reinforcement for elements subjected to shear and flexural loads. In the meantime, several experimental investigations have been conducted to assess the behavior of glass-FRP (GFRP) rebars in compression members. Maranan et al. [23] investigated the bond performance of GFRP rebars in GPC using a direct pullout test. The results revealed that the exhibited bond strength was similar to steel-reinforced GPC.

Additionally, it was reported by Tobbi et al. [24] that the GFRP rebars could be used as longitudinal reinforcement for compression members on the condition of proper confinement to prevent buckling of the rebars. Thus, combining GFRP rebars with GPC can yield more sustainable structural members with enhanced durability and acceptable integrity [25].

Due to their elastic behavior, GFRP rebars work as springs bonded to the concrete. Upon removing the applied load, GFRP-reinforced columns could rebound to their original shape, which is beneficial in the case of temporary loads like earthquakes [26]. Compared to steel rebars, larger deformation capacities can also be attained using GFRP rebars. However, steel rebars have a higher modulus of elasticity, providing higher stiffness to compression members. Moreover, due to the characteristics of steel yielding, it can provide the cross-section with adequate ductility. Therefore, Hybrid steel/GFRP reinforcement was proposed by many researchers to make use of the merits of both GFRP and steel. Hybrid reinforcement could be efficiently utilized through a double-layer configuration with an inner steel layer and an outer GFRP layer, which protects steel bars from corrosion and increases confinement effects. This hybrid double-layer reinforcement approach has been introduced and tested in beams and columns, and it was found to provide better ductility, larger deflection capacities, and fewer maintenance requirements [27–30].

Another aspect is the concrete core confinement, which has been closely investigated in the past three decades. It is universally accepted that proper confinement enhances the concrete core's strength and ductility. Moreover, increasing the core compressive strength and enhancing its post-peak behavior change the stress distribution throughout the columns' cross-section. Thus, it could significantly enhance its flexural strength at high curvatures [31,32]. The model introduced by Mander et al. [32] to predict the stress-strain response of the confined core was adopted by many researchers to simulate the confinement effects analytically. Since then, several trials to adopt new models or modified versions of the original Mander model have been introduced [25,26,33–36]. The differences in confinement behavior of steel and GFRP reinforcement originate from how they interact with the concrete core lateral strain, which initiates the transverse reinforcement strains, stresses, and pressure. Steel confinement pressure rises with increasing concrete lateral strain until the confining rebar reaches its yield plateau. In that case, confining pressure remains constant throughout subsequent increases to the axial concrete strain [and the corresponding radial strains associated with bulging outwards]. On the other hand, FRP rebars provide a different confinement behavior as the confinement pressure increases with the concrete core expansion until the rupture of the FRP confining rebars is reached [31].

Another topic of interest in column design is slenderness and its necessity for second-order analysis. Continuous research and rapid development in the construction industry, even with the evolution in erection techniques, make it increasingly appropriate to design and construct more slender structural members. ACI 318 [37] defines slenderness limits for steel-reinforced concrete columns, beyond which secondary effects should not be ignored. Recently, analytical and experimental research trials were performed to evaluate a slenderness limit for GFRP-reinforced concrete columns [38]. To assess the slenderness effects accurately, a second-order analysis must be completed within the analysis/design process through which the structural element's load capacity can substantially deteriorate. Several research articles have proposed various techniques for second-order analysis [39–41]. The main differences among these methods can be limited to two general aspects: the forces' integration technique along the cross-section of the columns and the calculation of lateral deflection along the column's height.

GPC has been utilized in several construction projects, including buildings, aircraft pavements, and bridges [15,42,43], and there is a continuous interest in GPC research, which is expected to grow in the following decade. However, limited application attempts are provided in the literature [7], and GPC has not developed enough international acceptance due to the lack of structural design codes and design standards [2,8]. A scientometric review was conducted by Zakka et al. [7] to analyze the research focus on GPC and determine the current research gaps. GPC's mechanical properties characterization and potential applications were among the identified research gaps this study aims to tackle. Moreover, several researchers have introduced double-layer reinforcement, and its merits have been demonstrated [27–30]. However, no detailed analytical models were introduced to simulate the double-layer scenario. As such, an analytical model was developed to integrate different aspects in analyzing slender columns with double layers of reinforcement herein.

This research introduces a complete framework, including all aspects mentioned earlier, to simulate GPC columns with different reinforcement configurations using steel and/or GFRP rebars in double-layer reinforcement. Material and geometric nonlinearities [second-order, or P-Delta effects] are incorporated utilizing an iterative layer-by-layer integration scheme. In addition, the effects of adding steel and synthetic macro fibers to the GPC matrix are modeled. The column's cross-section is divided into three regions according to the expected confinement level (cover, outer core, and inner core).

This document organization is set in a reader-convenience approach that details the study results and discussions, considering overall paper brevity. The next section is the research significance, followed directly by a deterministic sensitivity analysis, interaction diagrams study, and conclusion. Two appendices are provided to support and clarify the assertions in this paper. Appendix A details the constitutive relationships used, analytical model integration, and verification examples. Appendix B lists a large group of interaction diagram results summarized and discussed in this paper.

RESEARCH SIGNIFICANCE

This study introduces a complete framework to generate interaction diagrams for GPC columns, considering slenderness effects, fiber reinforcement and confinement effects, and double-layer reinforcement. Reinforcement configurations include all-GFRP, all-steel, and Hybrid cases. An extensive sensitivity analysis is conducted to substantially explore the effect of different design parameters on the bending moment and axial load capacities. The most influential parameters found in the analysis were selected to develop and investigate interaction diagrams under different slenderness ratios. In addition, the effects of fiber reinforcement on axial load development were explored. The findings of this study will help fulfill the current GPC research gaps identified by Zakka et al. [7] by providing a better understanding of slenderness and confinement effects on GPC and FRGPC columns with double layers of reinforcement. It also provides interaction diagrams that reflect secondary moment effects and slenderness ratio.

ANALYTICAL MODEL

Software written in Python [44] is developed to implement all theoretical assumptions for the targeted analytical model. A group of constitutive relations is integrated to account for confinement effects on GPC with and without steel/synthetic macro fibers. Stress-strain models for GFRP and steel reinforcements are incorporated into the model to complement stress simulation. The column's cross-section is divided into regions according to their confinement level. Then, a layer-by-layer discretization technique is adopted to integrate forces developed in each region. Equilibrium conditions are satisfied to develop moment-curvature load paths under different load-eccentricity values. Afterward, developed moment-curvature paths can be used to generate interaction diagrams.

The algorithms for calculating layers and rebars' geometric properties depend on the cross-sectional shape. The model applies to different cross-sections, including rectangular, triangular, T-, and L-sections with different reinforcement configurations. However, this paper focuses on the algorithms for calculating the properties of circular sections. Hence, verification examples and studies are provided only for circular sections in this research. The verification examples include validation against experimental results provided by Hales [26] and Hadi et al. [45], where circular columns were tested under different loading and testing configurations. Detailed information on model development, constitutive relationships, and verification examples are provided in Appendix A.

DETERMINISTIC SENSITIVITY ANALYSIS

The developed model incorporates multiple parameters that can potentially affect the behavior/response of columns under different loading conditions. To quantify the relative significance of these parameters, a deterministic sensitivity analysis was performed on different analysis groups with a set of pre-determined key parameters to be included. Inspecting these parameters allows for identifying their effects on different response measures in each analysis group. For these types of studies, tornado diagrams represent a proper tool to illustrate the results to facilitate identifying the impact of changing each parameter. Further details can be found in other studies, e.g., [46–49].

Considered Parameters

All the analytically investigated columns had a diameter of 440 mm with a double layer of longitudinal reinforcement laterally confined by spirals. All columns were assigned an initial plain concrete unconfined strength of 60 MPa. This means that for FRGPC, the effect of fiber reinforcement dosage is computed as indicated in Appendix A. The analysis included six groups with different reinforcing configurations, as depicted in Table 1. The elastic modulus and yield stress for steel reinforcement were 200 GPa and 420 MPa, respectively. Meanwhile, for the GFRP reinforcement, the elastic modulus and the ultimate tensile strength were 60 GPa and 1100 MPa, respectively. Upper and lower bounds of fiber reinforcement were based on the database given in the literature [20,50,51], and maximum v_f and l_f/d_f values were found to be 2.0% and 160, respectively. Thus, the upper bound for RI was taken to be 3.2 as the product of 160 and 2.0%. The maximum ρ_t was obtained by using the minimum allowable spiral spacing with the maximum practical diameter of a transverse reinforcement rebar. While the minimum ρ_t for steel was determined using Eq. (1) as per ACI-318 recommendations [37]. Table 2 summarizes the upper and lower bounds selected for different parameters.

$$\rho_t \geq 0.45\left(\frac{A_g}{A_{ch}} - 1\right)\frac{f_{co}}{f_y} \tag{1}$$

where A_{ch} is the area of the confined core measured to the outside edges of the transverse reinforcement.

Calculating the minimum allowable ρ_t for GFRP was achieved using Eq. (1) by replacing the steel yield strength, f_y, by the GFRP bent rebar strength, f_{fb}. It was found that the allowable minimum ρ_t for GFRP was lower than that for steel. However, it has been reported by Hadi et al. [52] that replacing steel reinforcement with the same amount of GFRP led to a reduction in the axial load-carrying capacity and bending moment. Thus, further research is recommended to inspect the minimum ρ_t that should be provided by GFRP, especially when used as a replacement of steel reinforcement.

Results and Discussions

Four output response values were recorded: the columns' axial load capacity, confinement efficiency, bending moment capacity, and the associated secant stiffness. As defined by Maranan et al. [25], the confinement efficiency (CE) was calculated as the ratio of the confined concrete strength to the unconfined concrete strength ($CE = f_{cc}/f_{cu}$). Fig. 1 presents the tornado diagrams of the sensitivity analysis results, which, in the following sections, will be expressed as percentages of the reference response values. The parameters will be listed in descending order according to their influence on the response in further discussions.

Axial Load Capacity

The sensitivity analysis results in Fig. 1a show that increasing all the parameters increased the axial load-carrying capacity for all groups and vice versa. For group GS1, the longitudinal reinforcement ratio (ρ_l) has shown to be the most influential parameter on the axial load capacity (from 85% to 127%). While concrete compressive strength (f_{co}), transverse reinforcement ratio (ρ_t), fiber reinforcing index (RI) resulted in ranges of (85% to 117%), (84% to 112%), and (86% to 110%), respectively. f_{co}, ρ_t, and RI have relatively comparable influence on the axial load capacity but lesser in comparison to ρ_l.

Group GS2, reinforced longitudinally and transversally with steel, has shown different behavior than group GS1. The most influential parameter was f_{co} with a range of (74% to 126%) while ρ_l, ρ_t, and RI resulted in ranges of (90% to 115%), (90% to 108%), and (92% to 107%), respectively. Having a hybrid reinforcement configuration, the response of group GS3 was expected to vary between those of GFRP and steel reinforcement. This was clear in the sensitivity results as the parameters f_{co}, ρ_l, ρ_t, and RI resulted in ranges of (81% to 124%), (89% to 119%), (87% to 111%) and (90% to 109%), respectively.

Regarding group GS4, the parameters ρ_l, f_{co}, ρ_t, and RI resulted in ranges of (86% to 129%), (85% to 120%), (83% to 114%), and (86% to 110%), respectively. Similar behavior was shown by GS1, which has the same initial configuration but with a different fiber content type. The axial load capacity sensitivity given by group GS5 has followed the same pattern and order as group GS2. The variation ranges were (73% to 128%), (89% to 116%), (91% to 108%), and (93% to 105%) for f_{co}, ρ_l, ρ_t, and RI, respectively. This similarity could be attributed to the only difference between GS2 and GS5: the macro fiber reinforcement type [synthetic instead of steel]. Following a similar behavior to group GS3, the parameters of group GS6 f_{co}, ρ_l, ρ_t, and RI resulted in ranges of (79% to 126%), (89% to 118%), (87% to 111%), and (91% to 107%), respectively.

Confinement Efficiency

The confined concrete strength is mainly dependent on the confinement configuration. However, as defined by Maranan et al. [25], confinement efficiency is a ratio of confined to unconfined concrete strength. Therefore, f_{co} was considered throughout the parameters affecting the confinement efficiency (CE). The CE results in (Fig. 1b) have shown a rather interesting response to changes in the input parameters. For all groups, increasing f_{co} and RI reduced CE, and vice versa, while increasing ρ_t and ρ_l increased CE, and vice versa. For group GS1, shifting from the lower bound to the upper bound of f_{co}, ρ_t, RI, and ρ_l produced a response change of (147% to 82%), (78% to 115%), (107% to 94%), and (98% to 101%), respectively.

The inverse behavior exhibited by f_{co} could be attributed to the fact that the high-strength concrete is not significantly affected by the confinement effects, as reported by Bing et al. [53]. Thus, increasing f_{co} or RI, which in turn increases f_{cu}, results in less sensitivity to the confinement effects. ρ_l was found to marginally impact CE. Unlike steel, GFRP reinforcement is not expected to directly affect CE, based on their governing model formulation. However, the indirect effects could be justified by reducing the inner concrete core diameter when larger longitudinal rebar diameters are used in the outer layer and vice versa.

Group GS2, all-steel reinforcement, showed similar behavior for f_{co}, ρ_t, RI, and ρ_l with variation ranges of (142% to 84%), (78% to 116%), (106% to 95%), and (98% to 101%), respectively. The amount of steel longitudinal reinforcement was found to be insignificant for CE. Following the same order of sensitivity, the variations were [(142% to 84%), (78% to 116%), (106% to 95%), and (98% to 101%)] for GS3, [(155% to 80%), (77% to 115%), (103% to 97%), and (98% to 101%)] for GS4, [(149% to 82%), (78% to 116%), (103% to 98%), and (98% to 101%)] for GS5, and [(149% to 82%), (78% to 116%), (103% to 98%), and (98% to 101%)] for GS6. There were marginal differences between the ranges of groups [GS2, GS3] and between those of [GS5, GS6]. However, due to the rounding of the percentages, several ranges remained virtually unchanged.

Bending Moment Capacity

The results of the bending moment capacity given in Fig. 1c show that all the groups demonstrated the same sensitivity order with similar patterns. Increasing all the parameters enhanced the bending moment capacity but not at the same rate. ρ_t parameter produced a negligible effect on enhancing the bending moment capacity. This could be attributed to the fact that, for the most part, a tensile-controlled failure is the most critical aspect affecting the columns' flexural capacity. Hence, the increase in core compressive strength associated with confinement effects does not significantly enhance flexural capacity.

For GS1, the ranges for ρ_l, f_{co}, and RI resulted in ranges of (47% to 151%), (87% to 111%) and (87% to 103%), respectively. Following the same sensitivity order, the response ranges were: (51% to 151%), (86% to 111%), and (82% to 104%) for GS2. While for GS3, they were: (47% to 155%), (88% to 111%), and (86% to 104%). For GS4, the corresponding ranges were: (43% to 154%), (86% to 112%), and (88% to 108%). As for GS5, they were: (45% to 155%), (85% to 112%), and (86% to 110%). Lastly, the respective ranges for GS6 were: (42% to 159%), (87% to 112%), and (87% to 108%).

Secant Stiffness

The secant stiffness was calculated as the peak moment divided by its corresponding curvature ($EI_{sec} = M/\phi$) [54]. Upon inspection of Fig. 1d, for GS1, the most influential parameters were ρ_l, f_{co} and RI with ranges (57% to 133%), (81% to 117%), and (88% to 105%), respectively. While ρ_t has marginally affected the secant stiffness at this load level.

One of the most notable findings from group GS2 was the secant stiffness values at the maximum bending moment scenario. Parameter ρ_l was the most influential, with a range of (47% to 146%). Parameters (f_{co}, RI, and the ρ_t) resulted in secant stiffness ranges of (64% to 99%), (105% to 72%), and (102% to 87%), respectively. The high limit for f_{co} had almost the same secant stiffness as the reference column. In addition, increasing RI and ρ_t resulted in the reduction of the secant stiffness, and vice versa. This behavior was not observed in the all-GFRP group [GS1]. The elastic behavior of GFRP bars allowed for an increase in bending moment, corresponding to a relatively moderate and proportional rise in curvature. Conversely, in the all-steel group [GS2], the moment increased with a much more significant increase in curvature due to steel yielding. Using the given definition of secant stiffness, it can be illustrated that $EI/EI_{reference} = (M/M_{reference})/(\phi/\phi_{reference})$. Thus, a reduction in the secant stiffness should be expected when the relative increase in curvature is manifested at a higher rate than at the moment.

Regarding GS3 and GS4, the behavior was like that of GS1 with parameters ρ_l, f_{co} and RI yielding ranges of [(57% to 137%), (82% to 116%), (87% to 104%)] for GS3, and [(54% to 135%), (80% to %119), and (88% to 107%)] for GS4. It was also found that ρ_t barely affected the secant stiffness. While for group GS5, the secant stiffness showed a different response to the input parameters. ρ_l and f_{co} resulted in ranges of (39% to 147%) and (58% to 106%), respectively. Conversely, an inverse pattern was found for RI with a range of (115% to 87%). It is worth noting that ρ_t resulted in a range of (95% to 102%) of the mean value. Compared to other groups, this unanticipated behavior could be attributed to the definition of secant stiffness, as discussed previously. i.e., a disproportionate increase in moment relative to curvature reduces the secant stiffness and vice versa. Finally, group GS6 showed similar behavior to that of GS1, GS3, and GS4 with ranges of (53% to 141%), (81% to 118%), and (88% to 107%) for ρ_l, f_{co} and RI, respectively.

INTERACTION DIAGRAMS

Considered Parameters

Based on the sensitivity analysis results, the most influential parameters were selected to explore the columns' interaction diagrams for varying slenderness ratios (KL/r). Nine combinational groups (GI1 to GI9) were assembled, as shown in Table 1, with three values of ρ_l per group (1%, 4%, and 8%). Additionally, three material strength levels (in Table 3) were investigated for both GFRP and steel reinforcement. For GFRP-reinforced layers, f_{fu} values were 900, 1000, and 1100 MPa, with respective corresponding E_f values of 40, 50, and 60 GPa.

Regarding steel-reinforced layers, the assigned f_y values per level were 420, 550, and 690 MPa, respectively, with a constant E_s of 200 GPa. Steel alloys associated with high yield strength values (550 to 760 MPa) typically exhibit a considerable strain hardening behavior [55]. However, for practical design considerations, since no strain hardening is considered by design standard, any steel grade with identifiable yield strength could be implemented in this model. Ergo, the selection of f_y values considered herein were subjected to the design limitations and conditions introduced in the ACI code [37].

Spirals were used to achieve ρ_t of 3.5%, while for columns with fiber reinforcement, an RI = 1.7 was deemed appropriate and representative. The parameters RI and ρ_t were not varied since it is beneficial to focus on the most influential parameters previously identified by the sensitivity analysis. More than 9,000 column configurations were analytically investigated during the development of the produced interaction diagrams. The complete set of results was tabulated and made publicly available on an online data repository [56]. More details regarding the analysis parameters and results can be found in [57].

Results and Discussions

For analytical investigation purposes, axial load and bending moment interactions are developed using nominal capacities. Thus, for design purposes, the environmental reduction factor for exposure conditions (C_E) and the strength reduction factor (Φ) should be incorporated. The reduction factor, C_E, is proposed by ACI 440.1R-15 [58] to reduce the guaranteed tensile strength of FRP rebars to the design level tensile strength. While Φ is the typical strength reduction factor used to design for factored loads [37,58].

To make it more practical for design, the results were presented in normalized forms: normalized axial load is defined as $P_n/f_{co}A_g$ and normalized bending moment is defined as $M_o/f_{co}A_gD_{sec}$. Where A_g is the gross area of the column's cross-section. The normalized interaction diagrams per group are represented in Appendix B. For conciseness, a representative group of interaction diagrams collected from groups GI1 through GI9 is included in the discussion, as shown in Fig. 2.

Influence of the longitudinal reinforcement ratio

The groups with all-GFRP reinforcement have shown a significant increase in the axial load capacity associated with increasing ρ_l. The all-steel reinforcement groups demonstrated the same behavior. However, the GFRP groups exhibited more sensitivity. This could be attributed to adequate confinement, which allowed the GFRP rebars to reach greater strains, thus generating higher load capacities. The increase of the bending moment capacity in the GFRP groups was also greater than that of the steel groups. The hybrid reinforcement groups showed a transitional behavior intermediary to all-GFRP and all-steel cases. However, the hybrid groups' sensitivity to the longitudinal reinforcement was closer to that of the steel groups. This can be attributed to the hybrid cases being always configured with an inner steel reinforced core that encloses most of the highly confined concrete inner core region.

It should be noted that the adopted model may have marginally overestimated the confining capabilities of the GFRP transverse reinforcement. This is directly attributed to the lack of conclusive evidence in the available literature on quantifying and adjusting for the somewhat inferior GFRP mechanical characteristics compared to steel (e.g., stiffness and bond strength). Nevertheless, the recalibrated model accounted for the bent-rebar strength reduction recommended in the ACI 440 standard [58]. This is widely accepted in the available literature [40]. However, further detailed experimental investigations are needed to better assess the strain compatibility conditions (or lack thereof) between concrete and GFRP transverse reinforcement. When that is achieved, it will allow for a more accurate representation of the strain compatibility conditions of the bulging concrete core and the surrounding GFRP transverse reinforcement.

Influence of slenderness ratio

The increase in the slenderness ratio has dramatically affected the columns' bending moment capacity. At high slenderness ratios with large eccentricities, the bending moment capacity suffered over 50% reductions, accompanied by a substantial decline in the axial load capacity. However, the groups with all-GFRP reinforcement groups suffered more losses in axial load capacities than their all-steel reinforcement counterparts. Upon increasing the slenderness ratio beyond the elastic buckling threshold, C_c, columns predominantly undergo elastic buckling. Such slender column behavior is characterized by overall geometric instability rather than material strength at the critical cross-section [59]. The maximum achievable axial load, in such cases, is the Euler buckling load, $P_E = EI(\pi/KL)^2$ which is governed by the elastic modulus and the second moment of area for the cross-section. This explains the lower axial load capacities of the slender all-GFRP columns compared to their all-steel counterparts. Since steel rebars have a higher elastic modulus than GFRP, steel rebars provide more considerable elastic stiffness to the column's cross-section.

Secant stiffness

The flexural secant stiffness ($EI_{analytical} = M/\phi$) for more than 800 GFRP reinforced columns were evaluated using the approach proposed in [60]. In which the secant stiffness is calculated at the onset of concrete cover spalling or the GFRP rebars reaching a strain value of 0.01, whichever is reached first. The results for columns with eccentricity ratios (e/D) ranging from 0.001 to 1.0 were compared to their theoretical counterparts ($EI_{theoretical}$) evaluated by definitions proposed in [60], and summarized in Appendix A. A histogram of $EI_{analytical}/EI_{theoretical}$ is presented in Fig. 3 for comparative purposes. It was found that the theoretical equation conservatively underestimates the secant stiffness for most columns with an average $EI_{analytical}/EI_{theoretical}$ ratio value of 2.61.

Effect of fiber reinforcement

Perhaps one of the most exciting insights observed was the effect of macro fiber reinforcement on the compressive behavior of unconfined concrete columns. Fig. 4a shows the stress-strain curves for two unconfined concrete specimens. The first specimen represents plain GPC, while the other is synthetic FRGPC with a fiber reinforcement index $RI = 0.2$. For each concrete type, two columns were analytically investigated using steel and GFRP longitudinal reinforcement. It can be seen how effective the fibers are in reducing the slope of the post-peak descending branch of the stress-strain curve. This behavior affects the evolution of the axial load-strain path to a threshold level, altering specific intrinsic material characteristics.

Fig. 4b represents the developed normalized axial load ($P_n/f_{co}A_g$) vs. strain curves of four analytically investigated columns with unique reinforcement properties. The exact value of initial concrete strength f_{co} was assigned to the four specimens. However, it can be seen that introducing the fiber reinforcement has resulted in two significant impacts. Firstly, the induced rise in the compressive strength of the synthetic FRGPC has increased the columns' axial load response at the early loading stages. Secondly, the post-peak behavior has entirely changed. The primary factor responsible for the pronounced occurrence of the conventional first peak shape was the cover spalling represented by the steep post-peak decline of the unconfined concrete. However, the presence of fibers mitigated that decline, which resulted in maintaining the axial load evolution without any drop at the cover cracking phase. Fig. 4c shows the participation of different columns` components in integrating the total axial load capacity. It is worth noting that similar findings were reported in published experimental investigations, e.g., [61].

CONCLUDING REMARKS

A meticulously verified capability was demonstrated to model circular columns' confinement and slenderness effects accurately. The presented analytical model was specially formulated for macro fiber-reinforced GPC columns with all-steel, all-GFRP, and steel/GFRP hybrid double-layered reinforcements. The model is generalizable and can easily be further extendable to accommodate a broader range of possibilities. e.g., more cross-sectional shapes, more sophisticated material models, and explicit consideration for bond-slip behavior. Based on the conducted limited-scope investigation, the following conclusions can be drawn:

- The macro fiber reinforcement of GPC has been shown to drastically delay cover spalling and significantly reduce its effects on compressive behavior. This is manifested through the apparent reduction in the steepness of the post-peak descending branch of the stress-strain relationship. In some instances, during the axial load evolution, it prevents the emergence of the substantial descending portion following the first peak. i.e., a higher second peak is achieved upon increasing axial strains beyond the initial cracking, damage, or softening, which are not accompanied by spalling.
- An extensive deterministic sensitivity analysis was conducted. The concrete compressive strength was the most influential parameter on the axial load capacity of all-steel and hybrid reinforced columns. The all-GFRP reinforced columns were primarily sensitive to the longitudinal reinforcement ratio.
- For all considered groups, the confinement efficiency was most sensitive to the concrete compressive strength, whereas the bending moment capacity was most sensitive to the longitudinal reinforcement ratio.
- The effective secant stiffness at the maximum bending moment was most sensitive to the longitudinal reinforcement ratio. An exciting insight into the unique behavior of all-steel

reinforced columns: increasing the concrete compressive strength resulted in a decreased secant stiffness. The higher concrete compressive strength resulted in a smaller compressive area. i.e., shallower neutral axis depth from the utmost compression fibers to the neutral axis, at ultimate. This effect increases bending moment capacity as well as curvature. However, curvature increases at a higher rate than the bending moment. As such, it decreases the secant stiffness.

- An extensive design interaction diagram set was developed for several reinforcement configurations combined with different slenderness ratios. It was observed that the all-GFRP reinforced columns were more sensitive to the longitudinal reinforcement ratio when compared to their all-steel reinforced counterparts. This could be attributed to the essentially elastic behavior of the GFRP bars. It enables them to continue providing increased strength to the confined core at higher axial strain levels than their yielding counterparts (steel reinforcement).
- All-GFRP reinforced columns were more sensitive to slenderness effects. This could be attributed to their inherently lower stiffness due to their lower elastic modulus than steel.
- Secant stiffness has been evaluated for over 800 columns and compared against theoretical calculations proposed in the literature [60]. Results have shown that theoretical calculations for most columns conservatively underestimate the secant stiffness, with an average $EI_{analytical}/EI_{theoretical}$ ratio value of 2.61.
- The presented model has demonstrated its capability of providing novel and profound insights for double-layered slender columns and confirming and asserting existing understanding of their expected behavior. This indicates the model’s capability to investigate additional practical scenarios further. e.g., double-layered reinforced Ultra-High Performance Concrete (UHPC) slender columns, High-Strength Steel (HST) reinforcement.

DATA AVAILABILITY STATEMENT

All data generated or used during the study are available in an online repository in accordance with funder data retention policies. [56] “Interaction Diagrams of Geopolymer FRC Slender Columns with Double-Layer Reinforcement_Dataset,” Zenodo. https://doi.org/10.5281/zenodo.10421691. Moreover, a data paper is available for further details regarding analysis inputs and the interpretation of the results [57]. All models and codes generated or used during the study are available from the corresponding authors upon reasonable request.

ACKNOWLEDGMENTS

This research was financially supported by the American University of Sharjah (AUS) through the Enhanced Faculty Research Grant program (EFRG18-MSE-CEN-25). The financial support is greatly appreciated. This paper represents the opinions of the authors and does not mean to represent the position or opinions of AUS. The authors would like to thank Mr. Hazem Kassab and Mr. Ahmed Maky for their involvement in the initial stages of the project.

NOTATION

All the symbols mentioned in the manuscript and appendices are explained in detail within their context. However, for reader convenience, all symbols and definitions are listed here:

A_{cc} = Net area of confined concrete.

A_{ch} = Area of the confined core measured to the outside edges of the transverse reinforcement.

A_e = Area of the effectively confined concrete core.

A_g = Gross area of the concrete cross-section.

$A_{l,i}$ = Area of the i^{th} rebar/strip within region l.

A_{lr} = Total area of the longitudinal reinforcement.

A_{sp} = The cross-sectional area of the spiral/hoop.

C_c = A slenderness ratio, identifying the elastic buckling threshold.

C_E = Environmental reduction factor for exposure conditions.

CE = Confinement efficiency.

D_{sec} = Diameter of the column's cross-section.

E_c = Elastic modulus of GPC.

E_{cf} = Elastic modulus of FRGPC.

E_{cu} = Elastic modulus of GPC/FRGPC.

E_f = Elastic modulus of GFRP rebars.

E_s = Elastic modulus of steel rebars.

EI_{sec} = Secant (effective) stiffness of moment-curvature path.

$EI_{theoretical}$ = Secant stiffness value proposed by [60].

$F_{l,i}$ = Axial force of the i^{th} rebar/strip within region l.

I_f = Moment of inertia of the GFRP reinforcement about the centroidal axis.

I_g = Moment of inertia of the columns` gross cross-sectional area.

K_e = Confinement effectiveness coefficient.

KL = Column's effective buckling length.

M_0 = The moment at the column's ends.

KL/r = Slenderness ratio.

M_{max} = Maximum bending moment through M-ϕ curve.

M_{mid} = Bending moment at the column's mid-height.

M_n = Nominal bending moment of the column's cross-section.

P = The axial compressive force applied at the column's ends.

P_E = Euler critical buckling load.

P_n = Nominal axial load of the column's cross-section.

R_{in}^l = Inner radius of region l.

$R_{l,i}$ = Distance from bar no. i in region l to the column's cross-section centroid.

R_{ou}^l = Outer radius of region l.

R_t^l = Thickness of region l.

RI = Fiber reinforcing index.

Y_n = Total eccentricity at the column’s mid-height cross-section.

$b_{l,i}$ = Width of strip i in layer l.

c = Depth of the neutral axis measured from the outermost compression edge.

d_b = Diameter of the bent GFRP bar.

d_f = Diameter of the steel/synthetic fibers.

$d_{l,i}$ = Depth of strip/rebar i in layer l.

d_s = Diameter of the confined core measured between the confining rebar centers.

e_0 = Eccentricity of applied axial load at column’s ends.

f_b = Stress in the rebar for a given strain ε_b.

f_{fb} = GFRP bent bar strength.

f_{fu} = Ultimate tensile strength of GFRP rebars.

f_l = Confinement pressure provided by steel or GFRP spirals/hoops.

$f_{l,i}$ = Axial stress of the i^{th} rebar/strip within region l.

f_c = Axial concrete strain corresponding to ε_c.

f_{cc} = Confined GPC/FRGPC concrete strength.

f_{cf} = Unconfined FRGPC strength.

f_{co} = Unconfined GPC strength.

f_{cu} = Unconfined GPC/FRGPC strength, i.e., f_{cf} or f_{co}.

f_r = Modulus of rupture for concrete.

f_t = Concrete tensile stress corresponding to a tensile strain ε_t.

f_y = Yield stress of steel rebars.

l_f = Length of the steel/synthetic fibers.

n_b^l = number of rebars in region l.

n_c = Curve fitting parameter for unconfined GPC.

n_{cc} = Curve fitting parameter for confined GPC/FRGPC.

n_{cf} = Curve fitting parameter for unconfined FRGPC.

n_{cu} = Curve fitting parameter for unconfined GPC/FRGPC.

n_s^l = number of strips in region l.

r = Coefficient for modeling unconfined GPC stress-strain.

r_b = The internal radius of the bent GFRP rebar.

s = Center to center spacing between hoop or spiral bars.

s' = Clear vertical spacing between hoop or spiral bars.

t_{sl} = Thickness of concrete strip l.

v_f = Fibers volumetric fraction content.

$y_{l,i}$ = y-coordinate of rebar i in region l, measured from section centroid.

α_f = Residual tensile strength of FRGPC.

δ_{mid} = Column's lateral mid-height deflection.

ε_b = Strain of reinforcement rebar.

ε_c = Axial compressive concrete strain.

ε_{cc} = Strain of confined concrete, corresponding to f_{cc}.

ε_{ce} = Compressive edge strain at the outermost fiber in the column's cross-section.

ε_{cf} = Strain of unconfined fiber-reinforced concrete, corresponding to f_{cf}.

ε_{cm} = Maximum attainable compressive edge strain for a short column.

ε_{co} = Strain of unconfined concrete corresponding to f_{co}.

ε_{cr} = Maximum attainable compressive edge strain for a slender column.

ε_{cu} = Strain of unconfined concrete corresponding to f_{cu}.

ε_{ft} = The ultimate tensile strain of GFRP spirals/hoops in micro-strain units.

ε_{ftcc} = Tie strain corresponding to the maximum compressive stress within the confined core.

ε_{fu} = Ultimate strain of GFRP rebars.

$\varepsilon_{l,i}$ = Axial strain of strip i in region l.

ε_t = Axial tensile concrete strain.

ε_y = Yield strain of steel rebars.

Φ = Design strength reduction factor.

ϕ_{mid} = curvature at the column's mid-height.

η_θ = Fibers' orientation factor.

ρ_l = Longitudinal reinforcement ratio.

ρ_t = Transverse reinforcement ratio.

θ = Angle for rebars/strips properties calculation.

REFERENCES

[1] Davidovits J. Geopolymers: Inorganic polymeric new materials. J Therm Anal 1991;37:1633–56. https://doi.org/10.1007/bf01912193.

[2] Ma C-K, Awang AZ, Omar W. Structural and material performance of geopolymer concrete: A review. Constr Build Mater 2018;186:90–102. https://doi.org/10.1016/j.conbuildmat.2018.07.111.

[3] Duxson P, Fernández-Jiménez A, Provis JL, Lukey GC, Palomo A, van Deventer JSJ. Geopolymer technology: the current state of the art. J Mater Sci 2007;42:2917–33. https://doi.org/10.1007/s10853-006-0637-z.

[4] Komnitsas KA. Potential of geopolymer technology towards green buildings and sustainable cities. Procedia Eng 2011;21:1023–32. https://doi.org/10.1016/j.proeng.2011.11.2108.

[5] Nath P, Sarker PK. Effect of GGBFS on setting, workability and early strength properties of fly ash geopolymer concrete cured in ambient condition. Constr Build Mater 2014;66:163–71. https://doi.org/10.1016/j.conbuildmat.2014.05.080.

[6] Saranya P, Nagarajan P, Shashikala AP. Development of ground-granulated blast-furnace slag-dolomite geopolymer concrete. ACI Mater J 2019;116:235–43.

https://doi.org/10.14359/51716981.

[7] Zakka WP, Abdul Shukor Lim NH, Chau Khun M. A scientometric review of geopolymer concrete. J Clean Prod 2021;280:124353. https://doi.org/10.1016/j.jclepro.2020.124353.

[8] Hassan A, Arif M, Shariq M. Use of geopolymer concrete for a cleaner and sustainable environment – A review of mechanical properties and microstructure. J Clean Prod 2019;223:704–28. https://doi.org/10.1016/j.jclepro.2019.03.051.

[9] Duxson P, Provis JL, Lukey GC, van Deventer JSJ. The role of inorganic polymer technology in the development of 'green concrete.' Cem Concr Res 2007;37:1590–7. https://doi.org/10.1016/j.cemconres.2007.08.018.

[10] Li Z, Ding Z, Zhang Y. DEVELOPMENT OF SUSTAINABLE CEMENTITIOUS MATERIALS. Beijing, China: 2004.

[11] Saranya P, Nagarajan P, Shashikala AP. Behaviour of GGBS-dolomite geopolymer concrete short column under axial loading. J Build Eng 2020;30:101232. https://doi.org/10.1016/j.jobe.2020.101232.

[12] Ismail I, Bernal SA, Provis JL, San Nicolas R, Brice DG, Kilcullen AR, et al. Influence of fly ash on the water and chloride permeability of alkali-activated slag mortars and concretes. Constr Build Mater 2013;48:1187–201. https://doi.org/10.1016/j.conbuildmat.2013.07.106.

[13] Byfors K, Klingstedt G, Lehtonen V, Pyy H, Romben L. Durability of Concrete Made With Alkali-Activated Slag. Third Int Conf Proceedings Fly Ash, Silica Fume, Slag, Nat Pozzolans Concr 1989:1429–66.

[14] Bakharev T, Sanjayan JG, Cheng Y-B. Sulfate attack on alkali-activated slag concrete. Cem Concr Res 2002;32:211–6. https://doi.org/10.1016/S0008-8846(01)00659-7.

[15] Zhang HY, Qiu GH, Kodur V, Yuan ZS. Spalling behavior of metakaolin-fly ash based geopolymer concrete under elevated temperature exposure. Cem Concr Compos

2020;106:103483. https://doi.org/10.1016/j.cemconcomp.2019.103483.

[16] Sarker PK, Kelly S, Yao Z. Effect of fire exposure on cracking, spalling and residual strength of fly ash geopolymer concrete. Mater Des 2014;63:584–92. https://doi.org/10.1016/j.matdes.2014.06.059.

[17] Junaid MT, Khennane A, Kayali O. Performance of fly ash based geopolymer concrete made using non-pelletized fly ash aggregates after exposure to high temperatures. Mater Struct 2015;48:3357–65. https://doi.org/10.1617/s11527-014-0404-6.

[18] Saranya P, Nagarajan P, Shashikala AP. Performance evaluation of geopolymer concrete beams under monotonic loading. Structures 2019;20:560–9. https://doi.org/10.1016/j.istruc.2019.06.010.

[19] Saranya P, Nagarajan P, Shashikala AP, Salam AP. Flexural Behaviour of GGBS-Dolomite Geopolymer Concrete Beams under Cyclic Loading. Mater Sci Forum 2019;969:291–6. https://doi.org/10.4028/www.scientific.net/MSF.969.291.

[20] Noushini A, Hastings M, Castel A, Aslani F. Mechanical and flexural performance of synthetic fibre reinforced geopolymer concrete. Constr Build Mater 2018;186:454–75. https://doi.org/10.1016/j.conbuildmat.2018.07.110.

[21] Farhan NA, Sheikh MN, Hadi MNS. Axial Load-Bending Moment (P-M) Interactions of Geopolymer Concrete Column Reinforced with and without Steel Fiber. ACI Struct J 2020;117:133–44. https://doi.org/10.14359/51720206.

[22] Elchalakani M, Ma G, Aslani F, Duan W. Design of GFRP-reinforced rectangular concrete columns under eccentric axial loading. Mag Concr Res 2017;69:865–77. https://doi.org/10.1680/jmacr.16.00437.

[23] Maranan G, Manalo A, Karunasena K, Benmokrane B. Bond Stress-Slip Behavior: Case of GFRP Bars in Geopolymer Concrete. J Mater Civ Eng 2015;27:04014116. https://doi.org/10.1061/(ASCE)MT.1943-5533.0001046.

[24] Tobbi H, Farghaly AS, Benmokrane B. Concrete Columns Reinforced Longitudinally and

Transversally with Glass Fiber-Reinforced Polymer Bars. ACI Struct J 2012;109:551–8. https://doi.org/10.14359/51683874.

[25] Maranan GB, Manalo AC, Benmokrane B, Karunasena W, Mendis P. Behavior of concentrically loaded geopolymer-concrete circular columns reinforced longitudinally and transversely with GFRP bars. Eng Struct 2016;117:422–36. https://doi.org/10.1016/j.engstruct.2016.03.036.

[26] Hales TA. SLENDER CONCRETE COLUMNS REINFORCED WITH FIBER REINFORCED POLYMER SPIRALS. PhD thesis, University of Utah, 2015.

[27] Hales TA, Pantelides CP, Reaveley LD. Experimental Evaluation of Slender High-Strength Concrete Columns with GFRP and Hybrid Reinforcement. J Compos Constr 2016;20:04016050. https://doi.org/10.1061/(ASCE)CC.1943-5614.0000709.

[28] Pang L, Qu W, Zhu P, Xu J. Design Propositions for Hybrid FRP-Steel Reinforced Concrete Beams. J Compos Constr 2016;20:04015086. https://doi.org/10.1061/(ASCE)CC.1943-5614.0000654.

[29] Osman SM, Wang Y, Alam MS, Sheikh SA. Nonlinear moment-curvature response of hybrid reinforced concrete sections using S-CALC. 12th Can. Conf. Earthq. Eng., 2019.

[30] Maranan GB, Manalo AC, Benmokrane B, Karunasena W, Mendis P, Nguyen TQ. Flexural behavior of geopolymer-concrete beams longitudinally reinforced with GFRP and steel hybrid reinforcements. Eng Struct 2019;182:141–52. https://doi.org/10.1016/j.engstruct.2018.12.073.

[31] Afifi MZ, Mohamed HM, Benmokrane B. Theoretical stress–strain model for circular concrete columns confined by GFRP spirals and hoops. Eng Struct 2015;102:202–13. https://doi.org/10.1016/j.engstruct.2015.08.020.

[32] Mander JB, Priestley MJN, Park R. Theoretical Stress-Strain Model for Confined Concrete. J Struct Eng 1988;114:1804–26. https://doi.org/10.1061/(ASCE)0733-9445(1988)114:8(1804).

[33] Karim H, Sheikh MN, Hadi MNS. Axial load-axial deformation behaviour of circular concrete columns reinforced with GFRP bars and helices. Constr Build Mater 2016;112:1147–57. https://doi.org/10.1016/j.conbuildmat.2016.02.219.

[34] Ganesan N, Abraham R, Deepa Raj S, Sasi D. Stress–strain behaviour of confined Geopolymer concrete. Constr Build Mater 2014;73:326–31. https://doi.org/10.1016/j.conbuildmat.2014.09.092.

[35] Muslikh, Anggraini NK, Hardjito D, Antonius. Behavior of Geopolymer Concrete Confined by Circular Hoops. MATEC Web Conf 2018;159:01018. https://doi.org/10.1051/matecconf/201815901018.

[36] Ahmad A, Plevris V, Khan Q-Z. Prediction of Properties of FRP-Confined Concrete Cylinders Based on Artificial Neural Networks. Crystals 2020;10:811. https://doi.org/10.3390/cryst10090811.

[37] ACI Committee 318. Building Code Requirements for Structural Concrete, ACI 318-19. Farmington Hills, MI :American Concrete Institute: 2019.

[38] Abdelazim W, Mohamed HM, Afifi MZ, Benmokrane B. Proposed Slenderness Limit for Glass Fiber-Reinforced Polymer-Reinforced Concrete Columns Based on Experiments and Buckling Analysis. ACI Struct J 2020;117:241–54. https://doi.org/10.14359/51718073.

[39] Abdelazim W, Mohamed HM, Benmokrane B, Afifi MZ. Effect of Critical Test Parameters on Behavior of Glass Fiber-Reinforced Polymer-Reinforced Concrete Slender Columns under Eccentric Load. ACI Struct J 2020;117:127–42. https://doi.org/10.14359/51723507.

[40] Hasan HA, Karim H, Sheikh MN, Hadi MNS. Moment-Curvature Behavior of Glass Fiber-Reinforced Polymer Bar-Reinforced Normal-Strength Concrete and High-Strength Concrete Columns. ACI Struct J 2019;116:65–75. https://doi.org/10.14359/51715573.

[41] Hales TA, Pantelides CP, Reaveley LD. Analytical buckling model for slender FRP-

reinforced concrete columns. Compos Struct 2017;176:33–42. https://doi.org/10.1016/j.compstruct.2017.05.034.

[42] Bligh R, Glasby T. Development of geopolymer precast floor panels for the Global Change Institute at University of Queensland. Proc. Concr. Inst. Aust. Bienn. Conf. Concr., 2013.

[43] CAO DG, Weng LQ, Wu YG. Study and Application of Quick Setting Early Strength Geopolymer Concrete. Sci Press 2015:(in Chinese).

[44] Van Rossum G, Drake FL. Python 3 Reference Manual. Scotts Valley, CA: CreateSpace; 2009.

[45] Hadi MNS, Ali S, Neaz Sheikh M. Experimental Study of GFRP-Reinforced Geopolymer Concrete Columns under Different Loading Conditions. J Compos Constr 2021;25. https://doi.org/10.1061/(ASCE)CC.1943-5614.0001164.

[46] Clemen RT. Making hard decisions: an introduction to decision analysis. Brooks/Cole Publishing Company; 1996.

[47] Porter KA, Beck JL, Shaikhutdinov R V. Sensitivity of Building Loss Estimates to Major Uncertain Variables. Earthq Spectra 2002;18:719–43. https://doi.org/10.1193/1.1516201.

[48] Binici B, Mosalam KM. Analysis of reinforced concrete columns retrofitted with fiber reinforced polymer lamina. Compos Part B Eng 2007;38:265–76. https://doi.org/10.1016/j.compositesb.2006.01.006.

[49] AlHamaydeh M, Abed F, Mustapha A. Key parameters influencing performance and failure modes for BRBs using nonlinear FEA. J Constr Steel Res 2016;116:1–18. https://doi.org/10.1016/j.jcsr.2015.08.038.

[50] Kazmi SMS, Munir MJ, Wu Y-F, Patnaikuni I, Zhou Y, Xing F. Axial stress-strain behavior of macro-synthetic fiber reinforced recycled aggregate concrete. Cem Concr Compos 2019;97:341–56. https://doi.org/10.1016/j.cemconcomp.2019.01.005.

[51] Farhan NA, Sheikh MN, Hadi MNS. Behavior of Ambient Cured Geopolymer Concrete

Columns under Different Loads. ACI Struct J 2018;115:1419–29. https://doi.org/10.14359/51702250.

[52] Hadi MNS, Karim H, Sheikh MN. Experimental Investigations on Circular Concrete Columns Reinforced with GFRP Bars and Helices under Different Loading Conditions. J Compos Constr 2016;20:04016009. https://doi.org/10.1061/(ASCE)CC.1943-5614.0000670.

[53] Bing L, Park R, Tanaka H. Stress-Strain Behavior of High-Strength Concrete Confined by Ultra-High- and Normal-Strength Transverse Reinforcements. ACI Struct J 2001;98:395–406. https://doi.org/10.14359/10228.

[54] Wight JK. Reinforced concrete: mechanics and design. 7th editio. Edinburgh Gate, Harlow, Essex CM20 2JE, England: Pearson; 2015.

[55] Charles G. Salmon, Johnson JE, Faris A. Malhas. Steel Structures: Design and Behavior. 5th ed. Upper Saddle River, New Jersey: PRENTICE HALL; 2008.

[56] AlHamaydeh M, Amin F. Interaction Diagrams of Geopolymer FRC Slender Columns with Double-Layer Reinforcement_Dataset V2. Zenodo 2023. https://doi.org/10.5281/zenodo.10421691.

[57] AlHamaydeh M, Amin F. Data for Interaction Diagrams of Geopolymer FRC Slender Columns with Double-Layer GFRP and Steel Reinforcement. Data 2021;6:43. https://doi.org/10.3390/data6050043.

[58] ACI Committee 440. Guide for the Design and Construction of Structural Concrete Reinforced with FRP Bars, ACI 440.1R-15. vol. 88 Reappro. Farmington Hills, MI :American Concrete Institute: 2015.

[59] Yoo CH, Lee SC. STABILITY OF STRUCTURES Principles and Applications. Elsevier Inc.; 2011.

[60] Abdelazim W, Mohamed HM, Benmokrane B. Proposed Flexural Stiffness of Slender Concrete Columns Reinforced with Glass Fiber-Reinforced Polymer Bars. ACI Struct J

2021;118:227–40. https://doi.org/10.14359/51728183.

[61] Farhan NA, Sheikh MN, Hadi MNS. Behaviour of Ambient Cured Steel Fibre Reinforced Geopolymer Concrete Columns Under Axial and Flexural Loads. Structures 2018;15:184–95. https://doi.org/10.1016/j.istruc.2018.07.001.

LIST OF TABLE CAPTIONS

LIST OF FIGURE CAPTIONS

LIST OF TABLES

Table 1. Material assignment for sensitivity analysis and interaction diagram groups.

Sensitivity Analysis Groups	Interaction Diagram Groups	Fiber Reinforcement Type	Longitudinal and Transverse Reinforcement	
			Outer layer	Inner layer
GS1	GI1	Steel	GFRP	GFRP
GS2	GI2	Steel	Steel	Steel
GS3	GI3	Steel	GFRP	Steel
GS4	GI4	Synthetic	GFRP	GFRP
GS5	GI5	Synthetic	Steel	Steel
GS6	GI6	Synthetic	GFRP	Steel
-	GI7	Plain	GFRP	GFRP
-	GI8	Plain	Steel	Steel
-	GI9	Plain	GFRP	Steel

Table 2. Key parameters used in the sensitivity analysis.

Input Parameter	Lower bound	Base value	Upper bound
Concrete compressive strength, f_{co} [MPa]	30	60	90
Fiber Reinforcement Index, RI	0.2	1.7	3.2
Long Reinforcement Ratio, ρ_l	1%	4%	8%
Transverse Reinforcement Ratio, ρ_t	3%	6%	9%

Table 3. Strength levels' assignment for interaction diagrams

Strength Level	GFRP Reinforcement		Steel Reinforcement	
	f_{fu} [MPa]	E_f [GPa]	f_y [MPa]	E_s [GPa]
1	900	40	420	200
2	1000	50	550	200
3	1100	60	690	200

LIST OF FIGURES

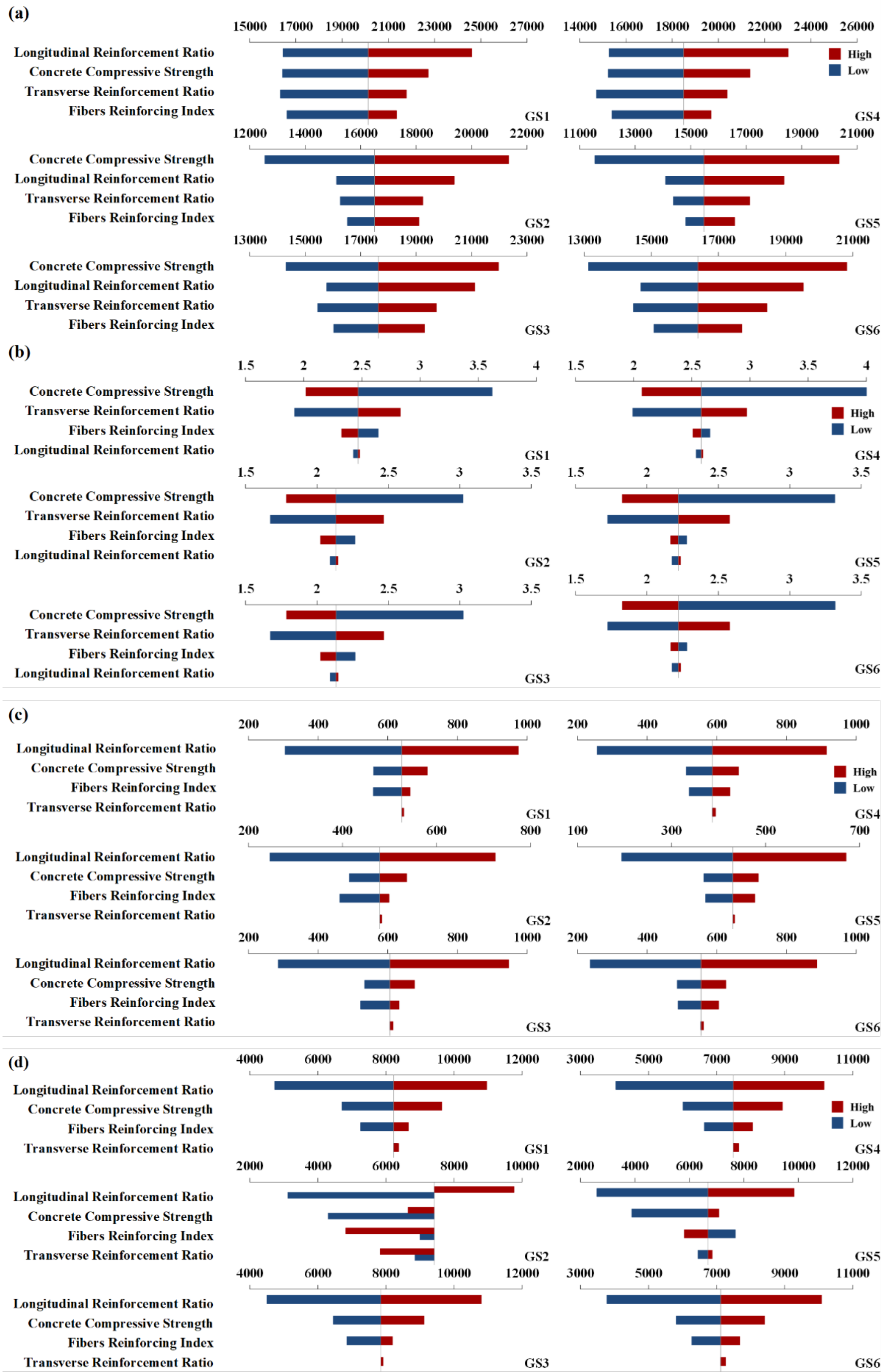

Fig. 1. Tornado diagrams of (a) axial load capacity [kN], (b) confinement efficiency, (c) bending moment capacity [kN. m], (d) secant stiffness [kN. m^2].

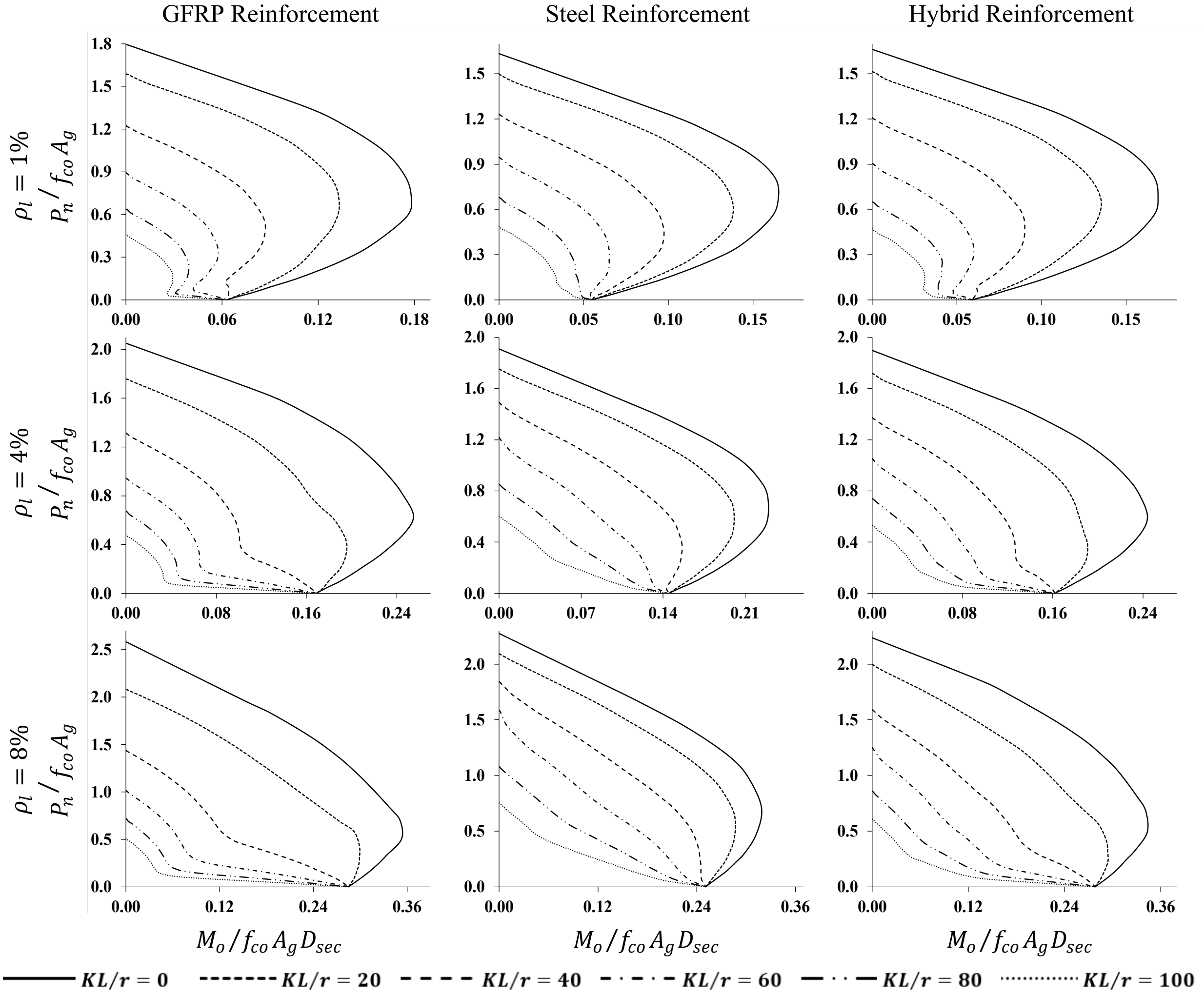

Fig. 2. The selected interaction diagrams for comparison.

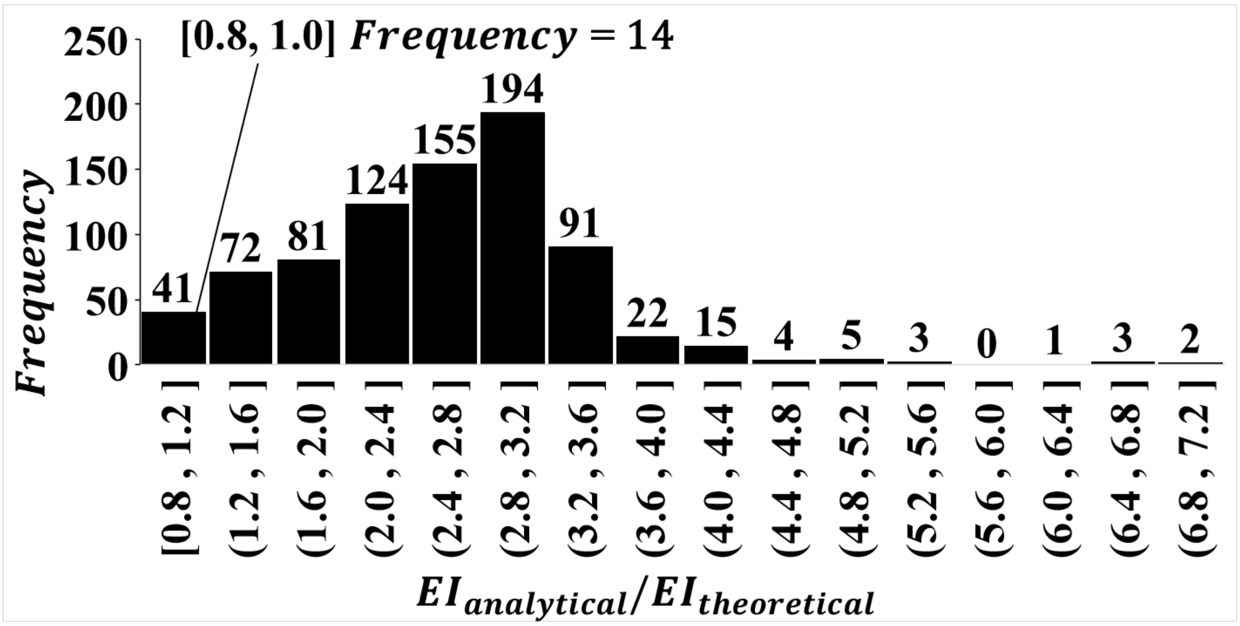

Fig. 3. Histogram of $EI_{analytical}$ values compared to the $EI_{theoretical}$ ones calculated as proposed by [60].

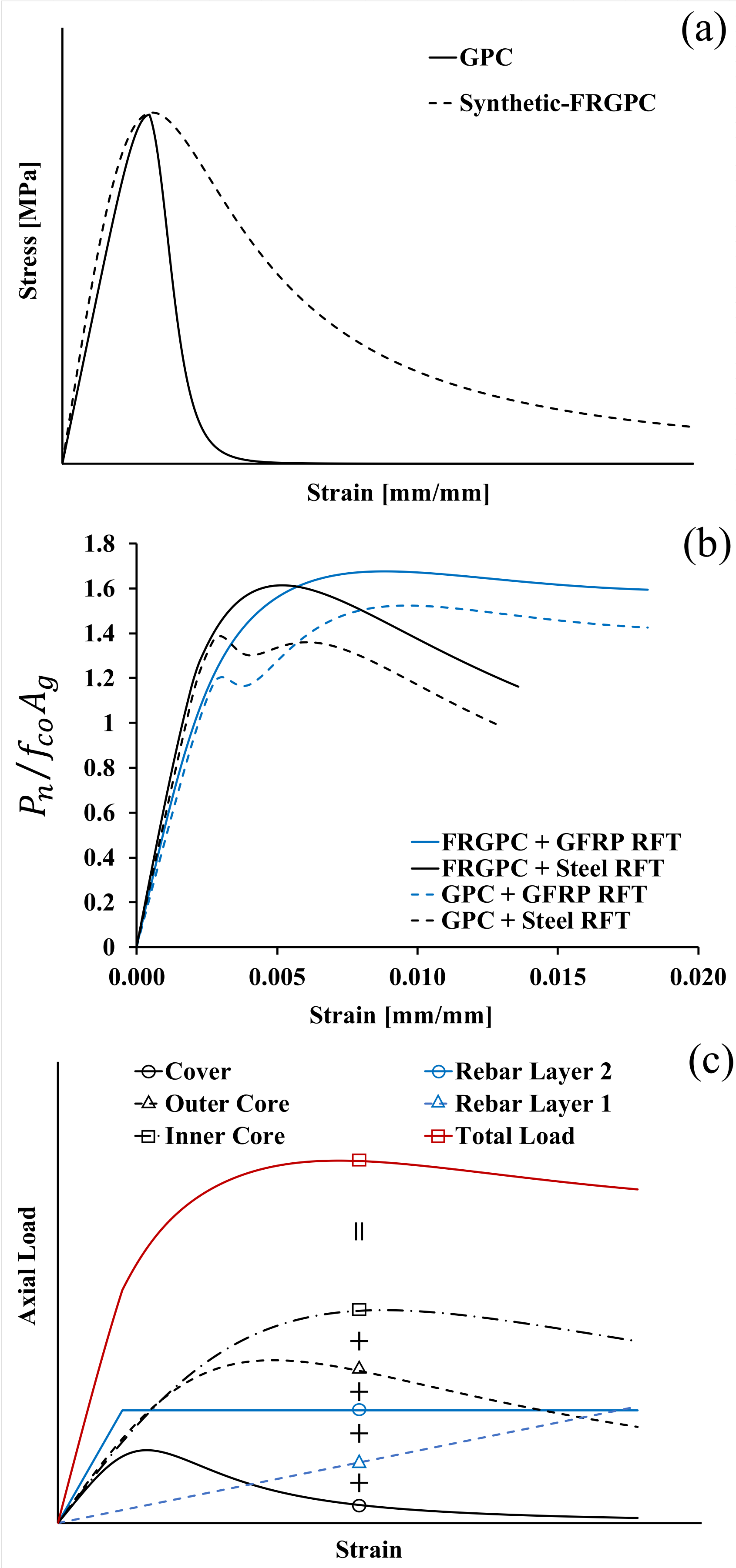

Fig. 4. Fiber reinforcement effects (a) typical stress-strain curves, (b) axial load evolution, (c) schematic diagram of participation of different column's components in axial load evolution.